Competition of Lattice and Basis for Alignment of Nematic Liquid Crystals

Andrew DeBenedictis and Timothy J Atherton*
Department of Physics and Astronomy, Tufts University, 574 Boston Avenue, Medford, MA 02155, USA

Candy Anquetil-Deck and Douglas J. Cleaver
Materials and Engineering Research Institute, Sheffield Hallam University, City Campus, Howard Street, Sheffield, S1 1WB, UK

David B. Emerson, Mathew Wolak, and James H. Adler
Department of Mathematics, Tufts University, 503 Boston Avenue, Medford, MA 02155, USA

Due to elastic anisotropy, two-dimensional patterning of substrates can promote weak azimuthal alignment of adjacent nematic liquid crystals. Here, we consider how such alignment can be achieved using a periodic square lattice of circular or elliptical motifs. In particular, we examine ways in which the lattice and motif can combine to favor differing orientations. Using Monte Carlo simulation and continuum elasticity we find, for circular motifs, that coverage fraction controls both the polar anchoring angle and a transition in the azimuthal orientation. If the circles are generalized to ellipses, arbitrary control of the effective easy axis and effective anchoring potential becomes achievable by appropriate tuning of the ellipse motif relative to the periodic lattice patterning. This has possible applications in both monostable and bi-stable liquid crystal device contexts.

I. INTRODUCTION

Surface anchoring, the promotion of a desired liquid crystal (LC) orientation by a surface [1], remains an important problem in applications because precise tuning of anchoring parameters is often necessary for optimal device performance [2]. Patterning the surface with a spatially varying preferred orientation is an attractive route to create alignment layers with desired anchoring properties because both the *effective* anchoring potential and its orientation or *easy axis* can be altered by adjusting geometric features of the pattern [3, 4]. Additionally, surfaces of appropriate symmetry [5] may promote multiple stable easy axes leading to *bistable* devices [6–9]. Bistability is desirable [10–13] both for reduced power consumption and improved addressing of high-resolution displays. Beyond displays, patterned LC systems are promising candidates as biosensors [14, 15] and photonic devices [16, 17].

Many methods exist to achieve patterning, encompassing both topographical and chemical approaches. These include mechanical rubbing [18, 19], photolithography [11, 18, 20], scribing with an atomic force microscope (AFM) [10, 21], microcontact printing of self-assembled monolayers (SAMs) [22–25], topographic surface features [26], and flexoelectric surface switching [27]. Since mechanical methods, such as rubbing, result in unwanted scratches or debris on the surface [28], and many methods do not scale well to high-volume manufacturing [25], SAMs have received much attention in recent years. Certain experimental methods show control over the azimuthal director angle as well as the polar anchoring angle [18, 29], and this is the focus of the work presented in this paper.

Striped surfaces, incorporating alternating regions preferring planar degenerate (lying parallel to the substrate but at any alignment angle) and homeotropic (perpendicular to the substrate) alignment, have been well studied [30–35]. For this pattern, the polar angle of the bulk LC is controlled by the average polar easy axis on the surface; the azimuthal alignment has an energy minimum aligned parallel or perpendicular to the stripe orientation depending on the ratio of the elastic constants [30]. Grooved surfaces with uniform alignment preference allow for similar control depending on the groove depth [36, 37]. Square checkerboard lattices are more complicated: an anchoring transition occurs in which the LC aligns with the lattice vectors for relatively strong surface anchoring, but switches to the diagonal for very weak anchoring [5]. Finally, both polar and azimuthal control over the bulk LC director orientation may be achieved with a rectangular checkerboard lattice. In this arrangement, certain rectangle ratios and anchoring strengths combine to shift the preferred director azimuthal angle from alignment with a rectangle edge to alignment diagonally across the rectangle [38].

For substrates constructed from squares or rectangles, the pattern units determine the symmetry and periodicity of the patterning. It is, however, straightforward to break this coupling by resorting to non-space-filling pattern basis motifs, such as circles or ellipses, and arranging these on a periodic lattice. Importantly, this approach provides a systematic approach by which to introduce the additional parameters needed to achieve truly independent control of polar and azimuthal anchoring angles and set these at arbitrary target values.

We employ a surface divided into two regions: the first is the space inside of an infinite array of ellipses, the centers of which form a square lattice, and whose as-

*Electronic address: timothy.atherton@tufts.edu

pect ratio and semi-major axis length and orientation are given. The second region is the space not contained within these ellipses. Each region is set to prefer either "vertical" (homeotropic) or "planar" (planar degenerate) alignment. The "vertical-on-planar" case corresponds to vertical alignment within the ellipses and planar alignment outside, while the "planar-on-vertical" case corresponds to planar alignment within the ellipses and vertical alignment outside. Two identical such surfaces bound our space in the z-direction. Fig. 3 shows the unit cell of this space for vertical on planar patterning.

In this paper, we use a continuum approach to determine the ground state of a LC in contact with this surface. From this, we identify scenarios for which the basis symmetry and the lattice symmetry may favor different alignments. This yields bistable configurations which are free from the constraints that exist for square or rectangular motifs. The paper is organized as follows: Monte Carlo (MC) simulation results with circle patterns are presented in section II. These motivate, in section III, an analytical continuum model which is constructed for this arrangement with the simplifying assumption that the director lies at a constant azimuthal angle. We also construct a numerical model that relaxes this assumption and explores the effect of saddle-splay. Brief conclusions are presented in section IV.

II. SIMULATIONS

The combination of MC simulations and continuum theory has proven synergistic in previous studies [5, 38]. The alignment induced by a particular pattern depends dramatically on the relative and absolute length scales present. The scenarios considered here contain three key lengths: the film thickness d, the radius of the circular (or elliptical) motif R, and the periodicity of that motif λ. While MC probes alignment around such patterns at the order of a few molecular lengths and continuum theory permits modeling up to device dimensions, the two approaches inform one another by identifying dominant regimes and thus highlighting their dependencies.

To gain a microscopic understanding of the effect of circle patterns on the adjacent nematic, we first performed MC simulations as described fully in [5]. Particle-particle interactions are modeled with the hard Gaussian overlap potential (HGO), in which the dependence of the interaction potential ν^{HGO} on $\hat{\mathbf{u}}_i$ and $\hat{\mathbf{u}}_j$, the orientations of particles i and j, and $\hat{\mathbf{r}}_{ij}$, the inter-particle unit vector is

$$\nu^{HGO} = \begin{cases} 0 & \text{if } r_{ij} \geq \sigma(\hat{\mathbf{r}}_{ij}, \hat{\mathbf{u}}_i, \hat{\mathbf{u}}_j) \\ \infty & \text{if } r_{ij} < \sigma(\hat{\mathbf{r}}_{ij}, \hat{\mathbf{u}}_i, \hat{\mathbf{u}}_j) \end{cases} \tag{1}$$

where $\sigma(\hat{\mathbf{r}}_{ij}, \hat{\mathbf{u}}_i, \hat{\mathbf{u}}_j)$ is the contact distance, is given by

$$\sigma(\hat{\mathbf{r}}_{ij}, \hat{\mathbf{u}}_i, \hat{\mathbf{u}}_j) = \sigma_0 \left[1 - \frac{\chi}{2} \left[\frac{\left(\hat{\mathbf{r}}_{ij}.\hat{\mathbf{u}}_i + \hat{\mathbf{r}}_{ij}.\hat{\mathbf{u}}_j\right)^2}{1 + \chi(\hat{\mathbf{u}}_i.\hat{\mathbf{u}}_j)} + \frac{\left(\hat{\mathbf{r}}_{ij}.\hat{\mathbf{u}}_i - \hat{\mathbf{r}}_{ij}.\hat{\mathbf{u}}_j\right)^2}{1 - \chi(\hat{\mathbf{u}}_i.\hat{\mathbf{u}}_j)} \right] \right]^{-1/2}. \tag{2}$$

The parameter χ is set by the particle length to breadth ratio κ via

$$\chi = \frac{\kappa^2 - 1}{\kappa^2 + 1}. \tag{3}$$

Particle-substrate interactions are modelled using the hard needle-wall potential (HNW) [39]. In this, the particles do not interact directly with the surfaces. Rather, the surface interaction is achieved by considering a hard axial needle of length $\sigma_0 k_s$ placed at the center of each particle. This gives an interaction

$$\nu^{HNW} = \begin{cases} 0 & \text{if } |z_i - z_0| \geq \sigma_w(\hat{\mathbf{u}}_i) \\ \infty & \text{if } |z_i - z_0| < \sigma_w(\hat{\mathbf{u}}_i) \end{cases} \tag{4}$$

where z_0 represents the location of a substrate and

$$\sigma_w(\hat{\mathbf{u}}_i) = \frac{1}{2}\sigma_0 k_s \cos(\theta_i). \tag{5}$$

Here, k_s is the dimensionless needle length and $\theta_i = \arccos(u_{i,z})$ is the angle between the substrate normal and the particle's orientation vector, which also corresponds to the zenithal Euler angle. For small k_s, the vertical arrangement has been shown to be stable, whereas planar anchoring is favored for long k_s [39]. Furthermore, despite its simplicity, the HNW potential has been found to exhibit qualitatively identical behavior to more complex particle-substrate potentials [40]. Here, by allowing k_s to vary across one wall, we investigate the molecular-scale effects of substrate patterning.

Simulations of HGO particles of aspect ratio $\kappa = 3$ were performed subject to confinement between two circle-patterned substrates with fixed separation d. Periodic boundaries were applied in x and y, with a common box edge length $L_x = L_y = L$. Sharp boundaries were imposed between vertical and planar regions, nee-

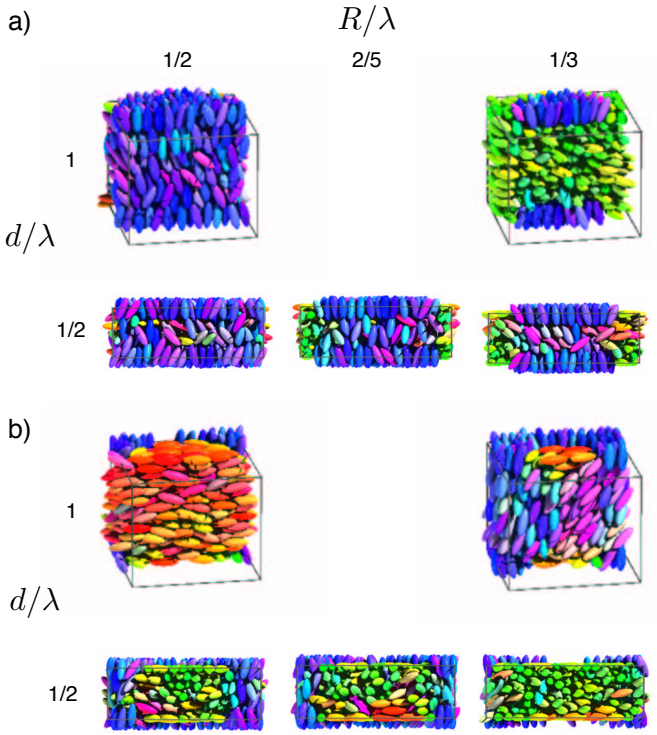

Figure 1: (Color online) Snapshots of Monte Carlo simulations of a nematic confined between periodically patterned circles. (a) Vertical-on-planar and (b) planar-on-vertical unit cells for different values of thickness d and circle radius R; the views show slices taken through the box mid-plane.

dle lengths $k_s = 0$ and κ, respectively, being specified in each region. Particle configurations were initialized at low density (i.e. large L) and uniformly compressed in the x and y dimensions by gradually reducing L between successive runs but maintaining the ratio R/L. An equilibration run of $N = 500,000$ MC sweeps was conducted at each density, followed by a production run of a further N sweeps. Orientational order was established when the number density at the center of the film reached that typical of the HGO nematic (i.e. $\simeq 0.32$). The corresponding in-plane box-length, L, then corresponded to the effective lattice periodicity λ.

As regards polar ordering, the findings of these simulations are summarized by the representative snapshots displayed in Fig. 1(a) for vertical-on-planar patterning; corresponding plots for the reverse case are in Fig. 1(b). These show that for $d = \lambda = 4\kappa\sigma_0$, the orientational ordering of the particles at the center of the film depends on R, the radius of the circle. For large R, the film follows the alignment of the particles in the circle, be that planar or vertical. However, a transition occurs with decreasing R, after which the orientation in the film becomes dictated by the pattern outside the circle. This behavior is observed for both vertical-on-planar and planar-on-vertical surfaces and essentially mimics that seen for other patterned films — the film orientation is dominated by that of the majority surface component.

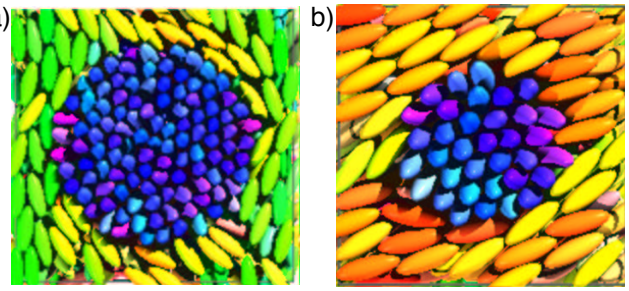

Figure 2: (Color online) Apparent orientational anchoring transition. a) Top configuration for vertical-on-planar patterning with $R/\lambda = 1/3$ and $d/\lambda = 1$. b) Top configuration for $R/\lambda = 1/4$.

Less intuitively, in all cases the surface patterning is limited to the at-substrate layers. As a result, even for these microscopically thin films, the dominant arrangement is that of a nematic monodomain. This is consistent with previous observations that, while stripe patterns can yield "bridging" of alternative orientational domains, 2-dimensional surface patterns are strictly confined to the surface monolayers [5, 38]. This tendency for the center of the film to follow the orientation of the majority pattern component persists down to very thin cells, such as $d = \lambda/2$, for which the film center can comprise as few as one layer of particles. In this regime, for the planar-on-vertical case (Fig. 1(b)), the particle orientation on the top and bottom substrates at a vertical-planar boundary is particularly interesting, because the particles tend to align parallel to the boundary, causing azimuthal distortion of the LC.

As well as showing that most pattern-confined LC films form nematic monodomains, MC simulations also indicate a more subtle azimuthal transition. As illustrated in Fig. 2 for the vertical-on-planar setup, the preferred azimuth of the planar region (which, in the cases depicted, is also the orientation of the underlying nematic monodomain) is also dependent on R. Specifically, for moderate-sized circles, the particles in the in-plane region align along the box x and y-axes, whereas at smaller R they pick out the box diagonal.

Two qualitative findings from these simulations, that films thicker than a few molecules form nematic monodomains and that there is a pattern-dependent azimuthal transition for vertical-on-planar systems, motivate and provide the focus for the continuum analysis that makes up the remainder of this paper.

III. CONTINUUM MODEL

In our continuum treatment, the LC orientation is characterized by a director field,

$$\mathbf{n} = (\cos\theta \sin\phi, \cos\theta \cos\phi, \sin\theta), \tag{6}$$

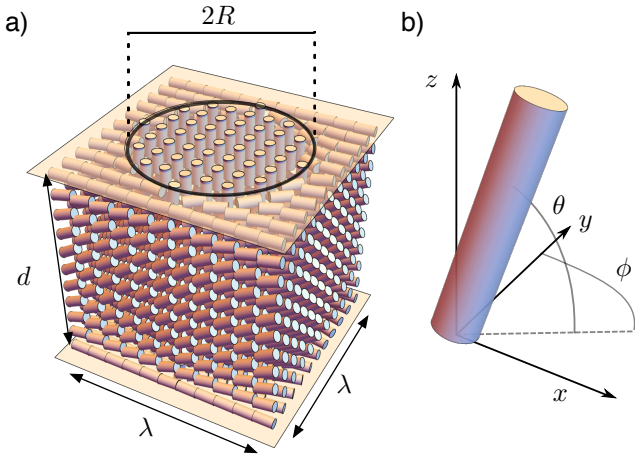

Figure 3: (Color online) (a) Schematic of the unit cell domain with important length scales labeled for a circle-patterned surface ($a = b = R$ and $\omega = 0$) with vertical-on-planar patterning. (b) Definition of the polar angle θ and the azimuthal angle ϕ of the LC director.

where θ is the zenithal angle and ϕ is the azimuthal angle. The free energy of the LC is the Frank free energy

$$F = \frac{1}{2}\int d^3x\,[K_1(\nabla\cdot\mathbf{n})^2 + K_2(\mathbf{n}\cdot\nabla\times\mathbf{n})^2 + K_3|\mathbf{n}\times\nabla\times\mathbf{n}|^2] + \int_S dS\, g(\theta-\theta_e), \quad (7)$$

supplemented by a harmonic anchoring potential

$$g(\theta-\theta_e) = \frac{W_\theta}{2}(\theta|_{z=\pm d/2} - \theta_e)^2. \quad (8)$$

The coordinates are set up as shown in Fig. 3: consider a unit cell defined on the box with corners at $(0, 0, -d/2)$ to $(\lambda, \lambda, +d/2)$. Each surface at $\pm d/2$ contains an ellipse centered on the unit cell with semi-major axis a oriented at an angle ω with respect to the x-axis and semi-minor axis b. The surfaces promote homeotropic ($\theta = \pi/2$) alignment within the ellipse and planar degenerate alignment ($\theta = 0$) outside.

A. Solution

Following previous work, we make the two-constant approximation by setting $K_1 = K_3$ and $K_2/K_1 = \tau$ [30]. Additionally, if the polar angle depends on all of the coordinates $\theta = \theta(x, y, z)$ and the azimuthal angle is constant in space $\phi = \phi_0$ [38], the bulk free energy may be rewritten as a quadratic form,

$$F = \frac{K_1}{2}\int (\nabla\theta)^T\cdot\mathbf{A}\cdot(\nabla\theta)d^3x + \frac{K_1}{2L_\theta\lambda}\int_S dS\,(\theta|_{z=\pm d/2} - \theta_e)^2 \quad (9)$$

where

$$\mathbf{A} = \begin{pmatrix} \frac{1}{2}(\alpha - \beta\cos 2\phi_0) & \frac{1}{2}\beta\sin 2\phi_0 & 0 \\ \frac{1}{2}\beta\sin 2\phi_0 & \frac{1}{2}(\alpha+\beta\cos 2\phi_0) & 0 \\ 0 & 0 & 1 \end{pmatrix}. \quad (10)$$

Here, we introduced the dimensionless polar anchoring parameter

$$L_\theta = \frac{K_1}{W_\theta\lambda}, \quad (11)$$

which may be recognized as a non-dimensionalized extrapolation length. The assumption of a constant azimuth is misleading in some geometries [41], but is corroborated by the monodomains seen in the MC simulations of this configuration.

Within this approximation, minimization of the free energy yields an anisotropic Laplace equation,

$$\nabla^T\cdot\mathbf{A}\cdot\nabla\theta(x, y, z) = 0, \quad (12)$$

where $\alpha \equiv 1 + \tau$ and $\beta \equiv 1 - \tau$. This may be solved using the series,

$$\theta(x, y, z) = \sum_{n,m=-\infty}^{\infty} 2A_{nm}\cosh(z/z_{nm})e^{i2\pi(nx+my)}, \quad (13)$$

where the penetration depth z_{nm} is defined by

$$z_{nm} = \left[2\pi^2\left(\alpha(m^2+n^2) + \beta(m^2-n^2)\cos 2\phi_0 + 2\beta nm\sin 2\phi_0\right)\right]^{-1/2}. \quad (14)$$

In order to satisfy the boundary conditions, the patterned easy axis is first expanded in a Fourier series,

$$\theta_e(x,y) = \sum_{n,m=0}^{\infty} S_{nm} e^{i2\pi(nx+my)}. \tag{15}$$

To determine the coefficients S_{nm}, we assume that the background surface promotes $\theta_e = 0$ while the elliptical pattern promotes $\theta_e = \pi/2$, or vertical-on-planar patterning; the alternative planar-on-vertical arrangement is trivially obtained from this solution by making the substitution,

$$\theta \to \pi/2 - \theta, \tag{16}$$

which leaves the energy invariant. The S_{nm} are therefore evaluated by integrating,

$$S_{nm} = \frac{\pi}{2} \iint_{\mathcal{D}} \exp\big(2\pi i(nx+my)\big) dxdy, \tag{17}$$

over a domain $\mathcal{D}$ defined by the ellipse equation,

$$(\vec{x}-\vec{x}_c)^T \mathbf{R}(\omega) \begin{pmatrix} 1/a^2 & 0 \\ 0 & 1/b^2 \end{pmatrix} \mathbf{R}(-\omega) (\vec{x}-\vec{x}_c) \leq 1. \tag{18}$$

Here, $\mathbf{R}(\omega)$ is the 2D rotation matrix and $\vec{x}_c = (\frac{1}{2}, \frac{1}{2})$ is the center of the ellipse. As shown in the appendix, the integral (17) can be performed analytically to yield,

$$S_{nm} = \frac{ab\pi}{2}(-1)^{n+m} \frac{J_1\left(2\pi\sqrt{a'^2_{nm} + b'^2_{nm}}\right)}{\sqrt{a'^2_{nm} + b'^2_{nm}}}, \tag{19}$$

where $J_1(x)$ is a Bessel function of the first kind, $a'_{nm} = (n\cos\omega + m\sin\omega)a$, and $b'_{nm} = (n\sin\omega - m\cos\omega)b$.

Having expanded the easy axis in a suitable form, the coefficients A_{nm} can be determined by imposing the Robin boundary condition [42] at $\pm d/2$.

$$\theta_e = \left[\pm L_\theta \frac{\partial\theta}{\partial z} + \theta\right]_{z=\pm d/2}, \tag{20}$$

Here, the $\pm$ refers to the direction of the outward normal to the LC boundary. Inserting Eqs. (13) and (15) into (20), we obtain,

$$A_{nm} = \frac{S_{nm}}{2\left(\frac{L_\theta}{z_{nm}}\sinh\left(\frac{d}{2z_{nm}}\right) + \cosh\left(\frac{d}{2z_{nm}}\right)\right)}. \tag{21}$$

Note that as $L_\theta \to 0$, this recovers the rigid anchoring condition. The solution for $\theta(x,y,z)$ is now obtained by inserting Eqs. (21), (19), and (14) into Eq. (13).

As for other patterns [5, 38], the director follows the surface pattern at $\pm d/2$, while relaxing to a uniform orientation, equal to the average polar angle promoted by the surface far away from the boundaries.

B. Circular patterns

For a circular surface pattern, set $a = b$ in Eq. (19). Evaluation of the volume integral in Eq. (7) then yields an expression for the bulk energy of the LC,

$$F_b = \sum_{n,m=-\infty}^{\infty} 2K_1 A_{nm}^2 \left[\mathbf{B}^T \mathbf{A} \left(\frac{d}{2}\,\mathrm{diag}(1,1,-1) + \frac{z_{nm}\sinh(d/z_{nm})}{2}\mathbf{I}_3\right)\mathbf{B}\right] \tag{22}$$

where

$$\mathbf{B} = \begin{pmatrix} 2\pi n \\ 2\pi m \\ 1/z_{nm} \end{pmatrix}.$$

Similarly, evaluation of the surface integral over the surfaces at $+d/2$ and $-d/2$ gives the surface energy of the LC,

$$F_s = \sum_{n,m=-\infty}^{\infty} \frac{K_1\left(S_{nm} - 2A_{nm}\cosh(\frac{d}{2z_{nm}})\right)^2}{L_\theta}. \tag{23}$$

The bulk and surface energy of the LC are shown in Fig. 4 as a function of the azimuthal angle ϕ for fixed circle radius and polar anchoring strength. The bulk energy always prefers alignment along the x- or y-axis, but with decreasing strength as the unit cell thickness decreases. Meanwhile, the surface energy prefers director alignment at a 45-degree angle to the axes. This surface preference grows slightly stronger as cell thickness decreases. It it noteworthy that, in spite of a planar degenerate surface condition, this configuration achieves non-degenerate anchoring. Results for planar-on-vertical patterning are identical due to the invariance of the energy under the linear transformation (16).

We estimate $W_{eff}(\phi)$, the effective azimuthal anchoring potential [43] as the energy difference per unit cell between the $\phi_0 = \phi$ and the $\phi_0 = 0$ states. A positive value

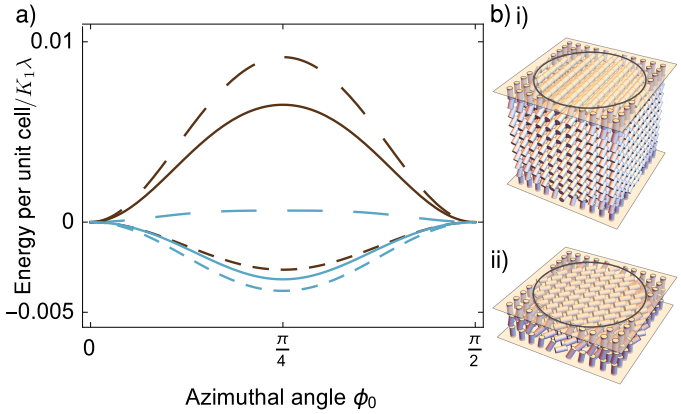

Figure 4: (Color online) (a) LC surface energy (dotted), bulk energy (dashed), and total energy (solid) as a function of the azimuthal angle for a unit cell of thickness $d/\lambda = 1.0$ (brown (darker gray)) and $d/\lambda = 0.25$ (cyan (lighter gray)) for planar-on-vertical patterning, $r/\lambda = 0.5$, and $L_\theta = 0.01$. For the thicker unit cell, the surface energy azimuthal preference is much weaker than that of the bulk and the overall preference aligns with that of the bulk. However, thinner cells exhibit weaker bulk energy preference and the total energy favors alignment along $\phi_0 = \pi/4$. (b) Corresponding calculated structures for i) $d/\lambda = 1.0$ and ii) $d/\lambda = 0.25$.

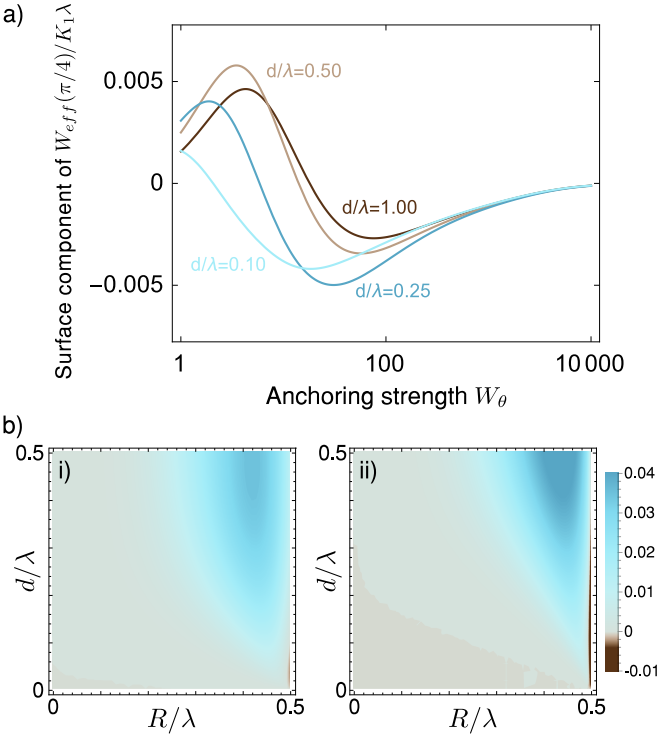

Figure 5: (Color online) (a) Surface energy as a function of polar anchoring strength W_θ for $R/\lambda = 0.5$ and several cell depths. As the cell depth decreases, the surface preference becomes more pronounced for a given value of W_θ. (b) Phase diagram showing the strength and orientation of the preferred azimuthal alignment angle as a function of cell depth d/λ and circle radius R/λ for i) $L_\theta = 0.100$, and ii) $L_\theta = 0.001$. Brown (bottom left and bottom right edge) regions indicate diagonal alignment $\phi_0 = \pi/4$ while cyan (top right) regions regions prefer alignment with the lattice vectors, $\phi_0 = 0$ or $\phi_0 = \pi/2$. The regions preferring diagonal alignment expand into larger cell depths as the anchoring strength increases.

of $W_{eff}(\phi)$ indicates a preference for alignment along the x- or y-axis, while a negative value of $W_{eff}(\phi)$ indicates a preference for alignment along ϕ. Correspondingly, we introduce the effective easy axis ϕ_p, which is the value of ϕ that minimizes the effective anchoring potential. For circular features, the effective easy axis is always either along a lattice vector ($\phi_p = 0$ or $\phi_p = \pi/2$) or along the diagonal ($\phi_p = \pi/4$). Fig. 5(a) shows the surface component of $W_{eff}(\pi/4)$ as a function of W_θ, the polar anchoring strength, for a series of cell thicknesses. The surface contribution is strongest for a thin cell with strong anchoring $W_\theta \approx 100$, which corresponds to $L_\theta = 0.01$. In the limit of rigid anchoring ($W_\theta \to \infty$) or extremely weak anchoring ($W_\theta \to 0$), the effective anchoring potential vanishes. For weak anchoring, the nematic effectively ignores the pattern, while for rigid anchoring the surface follows the prescribed pattern exactly.

To determine the parameter space in which parallel and diagonal alignment are each favored, we display in Fig. 5(b) the effective azimuthal anchoring potential $W_{eff}(\pi/4)$, shown for $L_\theta = 0.100$, and $L_\theta = 0.001$. The diagrams indicate two regions in which the the surface preference overrides the bulk preference for a sufficiently thin cell. The first of these is the regime found in the MC simulations (recall Fig. 2) on reducing the circle size R/λ. Fig. 5(b) confirms that the switch from parallel to diagonal alignment that occurs with decreasing circle radius is a general feature. Though the preference for diagonal alignment is very slight, it is readily observed by MC simulation. Simpler geometries have been found to also exhibit similar dependencies of bulk LC alignment on cell thickness and anchoring strength [44, 45]. The second region favoring diagonal alignment is the thin brown (bottom right edge) section at $R/\lambda = 0.5$, the largest possible circle radius.

A simple geometric observation explains the thin section: this region of parameter space is dominated by the surface term, due to the inability of x- or y-aligned LCs to effectively fill space between two abutting circles whose edges are nearly perpendicular to the LC director. Indeed, in this scenario, the planar regions closely approximate squares whose edges are aligned at $\pm\pi/4$. Less intuitive is the explanation for the light brown (bottom left) region that appears with decreasing circle size. Here, surface energy, dependent on the area of the surface features, decreases as the square of the surface feature length scale. However, because bulk energy depends on the area of the surface features times the penetration depth, which is fixed by the length scale of the feature, the bulk energy decreases as the cube of the surface feature length scale. Thus, decreasing feature size increases the relative influence of the surface preference.

The comparable magnitudes and conflicting preferences of the bulk and surface energies at these length scales indicate that combining lattice- and motif-contributions offers an interesting route to anchoring control. For these circular patterns, unlike the rectangular and square patterns previously considered, the alignment direction is promoted exclusively by the lattice while the motif favors no particular alignment. In the next subsection we therefore extend the capability of these systems by reducing the motif symmetry from circles to ellipses. This is done with the aim of determining how the anchoring behaviors already observed can be extended or achieved with greater control.

C. Elliptical patterns

We now consider elliptical patterns. For long ellipses, one might expect the effective azimuthal alignment to lie parallel to the semi-major axis, resembling the situation with alignment on striped surfaces[30]. Hence, by adjusting ω, it should be possible to control the effective azimuthal easy axis and, by tuning the aspect ratio, also control the effective azimuthal anchoring potential. The control parameter space to consider is greatly expanded: while the cell depth d/λ and the anchoring strength W_θ remain parameters, the circle radius R/λ is replaced by the semi major axis length b/λ, aspect ratio b/a, and the alignment angle ω. From the structure of the solution (13), we expect the cell depth and anchoring strength to have similar effects in both patterns and so we focus on the effects of the new parameters in this section.

In Fig. 6, we show effective azimuthal anchoring potentials $W_{eff}(\phi)$ calculated for a variety of values of ω and b/a. The coverage fraction of the pattern, or equivalently the area of the elliptical motif, is kept constant in order to fix the effective polar angle. An immediately obvious feature, compared to the equivalent profiles for circular patterns plotted in Fig. 4, is that the mirror symmetry of the pattern about $\phi = \pi/2$ is entirely broken, leaving behind a non-symmetric anchoring potential reminiscent of the structures fabricated in [46].

For fairly modest aspect ratios, the alignment angle of the ellipse controls the effective easy axis such that the energy minima occur at $\phi_p = \omega$. For smaller values of ω, or aspect ratios close to unity, the results are more complex: For instance, the effective easy axis for $\omega = \pi/8$ in Fig. 6(a) is $\phi_p = \pi/16$ instead of $\pi/8$. Also, in Fig. 6(b) we see that, for a rotation angle of $\pi/4$, the azimuthal effective easy axis moves from alignment with the sides of the unit cell to alignment with the semi major axis of the ellipse gradually, preferring $\phi_p = \pi/16$ for an aspect ratio of 1.05 and $\phi_p = \pi/8$ for an aspect ratio of 1.1.

The mechanism for this transition is two-fold. Firstly, the surface energy consistently prefers azimuthal alignment along the semi-major axis of the ellipse. Though the angle preferred by the surface remains the same for any non-unit aspect ratio, the strength of the preference grows with increasing aspect ratio. Second, as the aspect ratio grows, the bulk energy of the LC tends to prefer an azimuthal angle aligned with the ellipse alignment angle, but this move happens slowly such that small-to-moderate aspect ratios result in a preferred angle somewhere between $\phi_p = 0$ and $\phi_p = \omega$. The magnitude of the bulk energy preference also grows with increasing aspect ratio, but less dramatically than that of the surface energy preference.

The value of ϕ_p is therefore the result of a tension between surface and bulk effects. We display the effective easy axis and the effective anchoring potential as a function of aspect ratio in Fig. 7(a). For an alignment

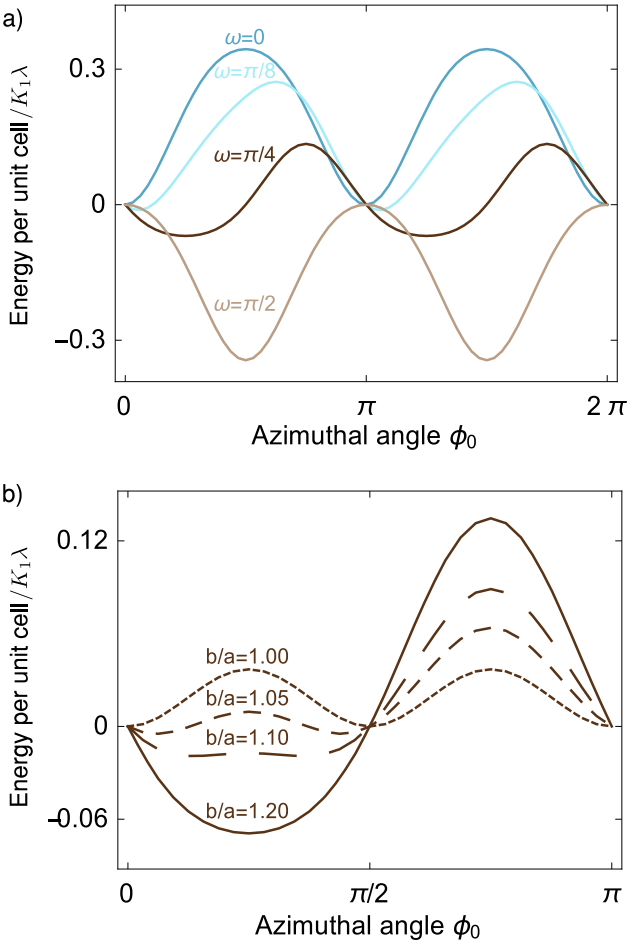

Figure 6: (Color online) Total LC energy as a function of the azimuthal angle shown for (a) several ellipse rotation angles with $b/a = 1.2$ and (b) for several different aspect ratios with $\omega = \pi/4$. Both panels have $d/\lambda = 1$, $L_\theta = 0.01$, and a coverage fraction equal to that of a circle with $R/\lambda = 0.4$. Rotation of the ellipse results in migration of the preferred azimuthal angle from alignment with the axes of the unit cell to alignment with the semi major axis of the ellipse. However, panel (b) shows that this transition in azimuthal angle preference is not immediate, but instead passes bistably through several smaller angles as aspect ratio increases.

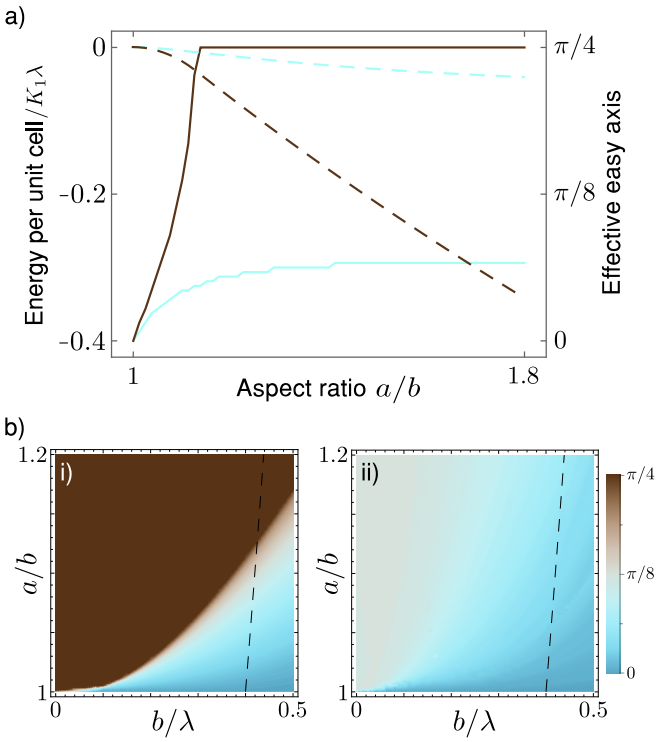

Figure 7: (Color online) (a) $W_{eff}(\phi_p)$ (dashed, left axis) and ϕ_p (solid, right axis) given a growing aspect ratio for ellipse alignment angles of $\omega = \pi/4$ (brown (dark gray)) and $\omega = \pi/8$ (cyan (light gray)) with $d/\lambda = 1$, $L_\theta = 0.01$, and a coverage fraction equal to that of a circle with $R/\lambda = 0.4$. (b) Phase diagram of ϕ_p as a function of aspect ratio b/a and semi major axis length b/λ with $d/\lambda = 1$ and $L_\theta = 0.01$ for ellipse rotation angles $\omega = \pi/4$ (i) and $\omega = \pi/4$ (ii). The dashed lines in (b) indicate the paths of constant coverage fraction followed in (a).

angle of ω=$\pi/4$, ϕ_p quickly aligns with the basis once the aspect ratio is increased above unity and $W_{eff}(\phi_p)$ increases linearly. For a more subtle rotation angle, ϕ_p rotates more slowly away from the lattice preference and does not reach alignment with the basis for any value of the aspect ratio that maintains the ellipse inscribed in the unit cell. Through this transition space, the magnitude of $W_{eff}(\phi_p)$ increases slowly due to the competition between bulk and surface preferences for azimuthal alignment.

Fig. 7(b) presents a phase diagram for the effective easy axis as a function of the semi-major axis and aspect ratio of the elliptical motifs while holding cell depth and anchoring strength constant. As expected, increasing aspect ratio leads to alignment of the effective easy axis with the ellipse long axis ($\phi_p = \omega$). Also, unit aspect ratios only achieve $\phi_p = 0$ at this depth, thus reproducing the behavior seen for circle patterns. We also note that, as seen in Fig. 5(b), smaller surface features allow for realization of the surface preference through the entire unit cell. In fact, panel (ii) indicates that a smaller coverage fraction does allow the effective easy axis to reach alignment with the basis, in contrast with the results of the larger feature in panel (a). Generally, for small to moderate-sized surface features, increases in aspect ratio quickly shift the LC azimuthal preference to align with the basis, overcoming the influence of the bulk.

Given the competition for LC alignment at the substrate layers, the constant-ϕ approximation may be too restrictive to characterize behavior at the surfaces of this system. The results of the MC simulations also suggest this: in the configurations shown in Fig. 1(b), the particles tend to align tangentially around the edge of the circle because for $\tau < 1$ the energetically cheapest way to achieve the vertical-to-planar transition around the perimeter of the circle is through a twist deformation. In section III D, therefore, we numerically minimize the free energy (7), plus a saddle-splay term, with respect to a completely arbitrary director profile to quantify the effect of azimuthal variations at each surface.

D. Numerical model

We performed a numerical minimization of the Frank energy (7) plus a saddle-splay term

$$f_{24} = -\frac{1}{2}(K_2 + K_{24}) \int d^3x \, \nabla \cdot (\mathbf{n}\nabla \cdot \mathbf{n} + \mathbf{n} \times \nabla \times \mathbf{n}) \quad (24)$$

to better capture the LC behavior at the top and bottom boundaries. Again, we assume $K_1 = K_3 \neq K_2$, and we set $K_{24} = (K_1 - K_2)/2$ per [47], but now the director is allowed to vary arbitrarily in 3D. A Cartesian representation of the director $\hat{n} = (n_x, n_y, n_z)$ was used and the unit length constraint $\hat{n} \cdot \hat{n} = 1$ enforced locally. The energy was discretized using second-order finite differences and minimized using an adaptive gradient-descent relaxation method with line searches. To improve convergence, successive refinement was used: an initial guess is relaxed on a coarse grid, then interpolated and relaxed onto successively finer grids. At each step, the system was relaxed until the energy converged.

Results from the relaxation model for a set of planar-on-vertical patterned surfaces are shown in Fig. 8(a). An initial guess with the director aligned along the y-axis was used. After relaxation, the director adopts an orientation tangent to the pattern edges, as seen in the corresponding MC simulations, Fig. 8(b). Similar behavior has been seen experimentally near the boundaries of nematics confined within curved curved geometries [48, 49]. The tangential alignment arises because it corresponds to a twist deformation across the vertical-planar boundary, which is energetically cheaper than a bend or splay deformation. The behavior breaks down for smaller circle radii because the bend deformation required to follow the arc of the feature becomes too energetically expensive. That this breakdown occurs at a larger radius in the MC runs owes to the fact that the K_3/K_1 ratio extracted from MC

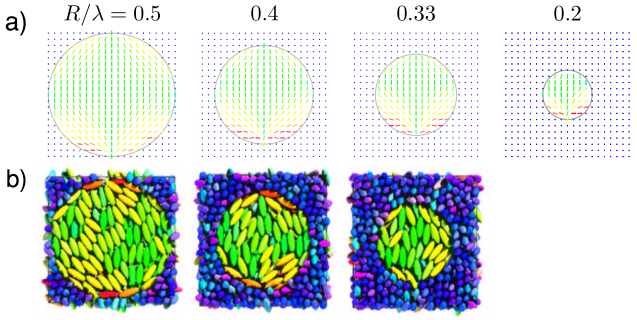

Figure 8: (Color online) (a) Results from 3D director minimization model. Shown is the director orientation on the bottom face of the unit cell for planar-on-vertical patterns of radius $R/\lambda = 0.5$, $R/\lambda = 0.4$, $R/\lambda = 0.33$, and $R/\lambda = 0.2$. These simulations are performed with $L_\theta = .001$, $d = 1.0$, a final grid size of $20 \times 20 \times 21$, and an initial guess that had the director aligned along the y-axis. (b) Corresponding results from Monte Carlo simulations.

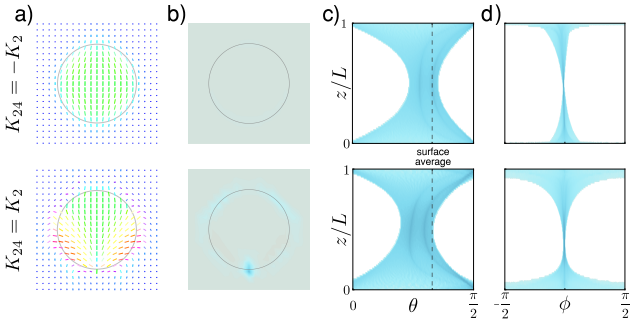

Figure 9: (Color online) Numerical results excluding saddle-splay (top) and including maximally strong saddle-splay (bottom) for planar-on-vertical patterning with $R/\lambda = 0.33$, $L_\theta = .01$, and $d = 1.0$. (a) Director orientation on the bottom face of the unit cell, (b) energy density on the bottom face of the unit cell (cyan/brown (darkest gray/darker gray) corresponds to positive/negative energy), (c) polar angle profile through the depth of the cell, and (b) azimuthal angle profile through the depth of the cell.

simulations of hard ellipsoids [50] is larger than the value of 1 used for the numerical relaxation.

In order to test the effect of the saddle-splay term, we also explore extreme K_{24} values as determined by the Ericksen-Leslie condition that $|K_{24}| \leq K_2$ [51]. Fig. 9 shows several results for $K_{24} = -K_2$ (top) and $K_{24} = K_2$ (bottom) with relatively weak surface anchoring. The director configurations of panel (a) show that strong saddle-splay inclusion serves to stabilize an escaped feature at the bottom of the circle motif. This effect is observable in panel (b) as well by the spike in the energy density near the bottom of the circle and the faint regions of negative energy density to the sides of the spike. This feature is reminiscent of the hedgehog structure commonly observed in experimental LC systems [52–54]. Under strong anchoring conditions ($L_\theta = 0.001$), the inclusion of saddle-splay has little effect, as expected.

The polar and azimuthal angle profiles of panels (c) and (d) indicate that the effect of K_{24} through most of the unit cell is nearly unobservable: relaxation of the director field away from the LC boundaries is slowed very slightly, but no meaningful qualitative difference exists away from the surfaces. We quantified the vector difference between director configurations at each gridpoint for these two cases as $1 - |\mathbf{n}_1 \cdot \mathbf{n}_2|$ and found the 50th and 95th percentiles to be 0.00498 and 0.0747. This confirms the monodomain findings of section II and supports both the exclusion of saddle-splay and the use of a constant azimuthal angle in our analytical results.

IV. CONCLUSION

This paper has considered the alignment behavior of square arrays decorated with elliptical motifs, demonstrating that such patterns can be used to create surfaces with controllable anchoring potential and easy axis by varying the period of the pattern, ellipse orientation, aspect ratio, and coverage fraction. Given the two-constant approximation and the assumption of a constant azimuthal angle, the director configuration and energy can be computed analytically. Depending on the circle radius, cell depth, and polar anchoring strength of the alignment material, the ground state may have azimuthal alignment along either of the lattice vectors, or diagonally.

Our study offers invaluable advice for applications because, while the elliptical patterned surface offers a remarkable degree of control over the anchoring properties, the design parameter space for the pattern is large. Briefly, surfaces patterned by rotated ellipses allow control of the azimuthal angle over a continuum of values between the lattice vectors and the diagonal depending on the orientation of the ellipse. In these cases, the ellipse aspect ratio controls the effective anchoring potential. The behavior is nontrivial, however, and includes regions of bistability, as well as an azimuthal anchoring transition for some designs.

Unlike for other patterned surfaces previously studied, the constant azimuthal angle approximation is only of limited use at the surfaces. A numerical study showed a preference for tangential alignment along the vertical-planar boundary of the pattern in excellent agreement with MC simulations. Also, the inclusion of a saddle-splay term in the Frank energy is found to promote formation of an escaped feature in the director field at one point on the circle motif.

While the present study has considered a flat surface, the results may also be important for experimentalists using arrays of tall posts to align LCs as has been reported in [55–57]. It seems that only a very modest amount of anisotropy in the shape of the pillars, for example using posts of elliptical cross section, may break the square symmetry and lead to significantly better azimuthal alignment if desired.

Acknowledgments

The authors wish to thank Tufts University for a Tufts Collaborates! seed grant that partly funded one of the co-authors (DBE). ADB was part funded by a Graduate Student Summer Scholarship from Tufts University. TJA is grateful to the Research Corporation for Science Advancement for a Cottrell Scholar Award.

Appendix

To evaluate the Fourier coefficients for the easy axis, first substitute $x \to x' + 1/2$ and $y \to y' + 1/2$, which allows (17) and (18) to be rewritten as

$$S_{nm} = \frac{\pi}{2} \exp\big(\pi i(n+m)\big) \iint_{\mathcal{D}} \exp\big(2\pi i(nx' + my')\big) dx'dy', \tag{25}$$

and

$$\left(\frac{x'\cos\omega + y'\sin\omega}{a}\right)^2 + \left(\frac{x'\sin\omega - y'\cos\omega}{b}\right)^2 \leq 1, \tag{26}$$

respectively. Note that the exponential pre-factor in (25) is $(-1)^{n+m}$ since n and m are integers.

Next, rotate the coordinates via the transformations $(x'\cos\omega + y'\sin\omega)/a \to x''$ and $(x'\sin\omega - y'\cos\omega)/b \to y''$, and integrate using these new coordinates,

$$S_{nm} = \frac{ab\pi}{2}(-1)^{n+m} \iint\limits_{(x'')^2+(y'')^2\leq 1} \exp\Big(2\pi i\big((n\cos\omega + m\sin\omega)ax'' + (n\sin\omega - m\cos\omega)by''\big)\Big) dx''dy''. \tag{27}$$

Define $a' = (n\cos\omega + m\sin\omega)a$, $b' = (n\sin\omega - m\cos\omega)b$, $\alpha = (a', b')$, and $g(s) = \exp(is)$ and convert to polar coordinates such that $(x'', y'') \to r\xi$ where $\xi = (\cos\theta, \sin\theta)$:

$$S_{nm} = \frac{ab\pi}{2}(-1)^{n+m} \int_0^1 r\, dr \int_\xi g(2\pi r\alpha\cdot\xi) d\xi. \tag{28}$$

Eqs. (1.2) and (1.5) from [58] allow us to evaluate the inner integral to find

$$S_{nm} = \frac{ab\pi}{2}(-1)^{n+m} \int_0^1 2\pi r J_0\left(2\pi r\sqrt{a'^2 + b'^2}\right) dr. \tag{29}$$

Finally, let $k = 2\pi\sqrt{a'^2 + b'^2}$ and $s = kr$, and note that $\int xJ_0(x)dx = xJ_1(x)$ to obtain,

$$\begin{aligned} S_{nm} &= \frac{ab\pi}{2}(-1)^{n+m}\frac{2\pi}{k^2}\int_0^k sJ_0(s)ds \\ &= \frac{ab\pi}{2}(-1)^{n+m}\frac{2\pi}{k}J_1(k) \\ &= \frac{ab\pi}{2}(-1)^{n+m}\frac{J_1\left(2\pi\sqrt{a'^2+b'^2}\right)}{\sqrt{a'^2+b'^2}}, \end{aligned} \tag{30}$$

the result stated in Eq. (19).

[1] B. Jerome, Rep. Prog. Phys. **54**, 391 (1991).

[2] T. J. Spencer and C. M. Care, Phys. Rev. E **74**, 061708

(2006).
[3] S. Kondrat, A. Poniewierski, and L. Harnau, The European Physical Journal E **10**, 163 (2003).
[4] G. Barbero, T. Beica, A. L. Alexe-Ionescu, and R. Moldovan, Journal de Physique II **2**, 2011 (1992).
[5] C. Anquetil-Deck, D. J. Cleaver, and T. J. Atherton, Phys. Rev. E **86**, 041707 (2012).
[6] J. H. Kim, M. Yoneya, J. Yamamoto, and H. Yokoyama, Appl. Phys. Lett. **78**, 3055 (2001).
[7] Y. W. Yi, V. Khire, C. N. Bowman, J. E. MacLennan, and N. A. Clark, J. Appl. Phys. **103**, 1 (2008).
[8] M. Yoneya, J. H. Kim, and H. Yokoyama, Appl. Phys. Lett. **80**, 374 (2002).
[9] B. Lee and N. A. Clark, Science **291**, 2576 (2001).
[10] J.-H. Kim, M. Yoneya, and H. Yokoyama, Nature **420**, 159 (2002).
[11] M. Stalder and M. Schadt, Liq. Cryst. **30**, 285 (2003).
[12] G. P. Bryan-Brown, Displays **27**, 37 (2000).
[13] S. Kitson and A. Geisow, Appl. Phys. Lett. **80**, 3635 (2002).
[14] D. K. Hwang and A. D. Rey, Soc. Ind. Appl. Math. **67**, 214 (2006).
[15] A. M. Lowe, B. H. Ozer, Y. Bai, P. J. Bertics, and N. L. Abbott, ACS Appl. Mater. Interfaces **2**, 722 (2010).
[16] L. Z. Ruan, J. R. Sambles, and I. W. Stewart, Phys. Rev. Lett. **91**, 033901 (2003).
[17] L. Wei, J. Weirich, T. T. Alkeskjold, and A. Bjarklev, Opt. Lett. **34**, 3818 (2009).
[18] I. H. Bechtold and E. A. Oliveira, Mol. Cryst. Liq. Cryst. **442**, 41 (2005).
[19] S. Varghese, S. Narayanankutty, C. W. M. Bastiaansen, G. P. Crawford, and D. J. Broer, Advanced Materials **16**, 1600 (2004).
[20] M. Schadt, K. Schmitt, V. Kozinkov, and V. Chigrinov, Japanese Journal of Applied Physics **31**, 2155 (1992).
[21] F. K. Lee, B. Zhang, P. Sheng, H. S. Kwok, and O. K. C. Tsui, Appl. Phys. Lett. **85**, 5556 (2004).
[22] V. K. Gupta and N. L. Abbott, Science **276**, 1533 (1997).
[23] Y. L. Cheng, D. N. Batchelder, S. D. Evans, J. R. Henderson, J. E. Lydon, and S. D. Ogier, Liq. Cryst. **27**, 1267 (2000).
[24] P. Prompinit, A. S. Achalkumar, J. P. Bramble, R. J. Bushby, C. Wälti, and S. D. Evans, ACS Appl. Mater. Interfaces **2**, 3686 (2010).
[25] W. Zheng, C.-Y. Chiang, and I. Underwood, Thin Solid Films **545**, 371 (2013).
[26] D. Liu, C. W. M. Bastiaansen, J. M. J. den Toonder, and D. J. Broer, Macromolecules **45**, 8005 (2012).
[27] C. Denniston and J. M. Yeomans, Phys. Rev. Lett. **87**, 275505 (2001).
[28] M. J. Park and O. O. Park, Microelectron. Eng. **85**, 2261 (2008).
[29] H. T. A. Wilderbeek, J. P. Teunissen, C. W. M. Bastiaansen, and D. J. Broer, Advanced Materials **15**, 985 (2003).
[30] T. J. Atherton and J. Sambles, Phys. Rev. E **74**, 022701 (2006).
[31] T. J. Atherton, J. R. Sambles, J. P. Bramble, J. R. Henderson, and S. D. Evans, Liq. Cryst. **36**, 353 (2009).
[32] T. Atherton, Liq. Cryst. **37**, 1225 (2010).
[33] M. Ledney and O. Tarnavskyy, Soft Matter **56**, 880 (2011).
[34] S. Kondrat, A. Poniewierski, and L. Harnau, Liq. Cryst. **32**, 95 (2005).
[35] Y. Yi and N. A. Clark, Liq. Cryst. **40**, 1736 (2013).
[36] D.-H. Chung, T. Fukuda, Y. Takanishi, K. Ishikawa, H. Matsuda, H. Takezoe, and M. A. Osipov, Journal of Applied Physics **92**, 1841 (2002).
[37] G. Barbero, A. S. Gliozzi, and M. Scalerandi, Journal of Applied Physics **104**, 094903 (2008).
[38] C. Anquetil-Deck, D. J. Cleaver, J. P. Bramble, and T. J. Atherton, Phys. Rev. E **88**, 012501 (2013).
[39] D. Cleaver and P. Teixeira, Chem. Phys. Letts. **338**, 1 (2001).
[40] F. Barmes and D. Cleaver, Phys. Rev. E **69**, 061705 (2004).
[41] J.-i. Fukuda, M. Yoneya, and H. Yokoyama, Phys. Rev. Lett. **98**, 187803 (2007).
[42] I. Stewart, *The Static and Dynamic Continuum Theory of Liquid Crystals: A Mathematical Introduction*, Liquid Crystals Book Series (CRC Press, 2004).
[43] L. Harnau, S. Kondrat, and A. Poniewierski, Phys. Rev. E **76**, 051701 (2007).
[44] A. Sparavigna, O. D. Lavrentovich, and A. Strigazzi, Phys. Rev. E **49**, 1344 (1994).
[45] P. Teixeira, Phys. Rev. E **55**, 2876 (1997).
[46] S. Ferjani, Y. Choi, J. Pendery, R. Petschek, and C. Rosenblatt, Phys. Rev. Lett. **104** (2010).
[47] H. Yokoyama, Phys. Rev. E **55**, 2938 (1997).
[48] O. V. Manyuhina, K. B. Lawlor, M. C. Marchetti, and M. J. Bowick, Soft Matter **11**, 6099 (2015).
[49] V. Jamali, N. Behabtu, B. Senyuk, J. A. Lee, I. I. Smalyukh, P. van der Schoot, and M. Pasquali, Phys. Rev. E **91**, 042507 (2015).
[50] B. Tjipto-Margo, G. T. Evans, M. P. Allen, and D. Frenkel, The Journal of Physical Chemistry **96**, 3942 (1992).
[51] J. L. Ericksen, Physics of Fluids **9**, 1205 (1966).
[52] G. Volovik and O. Lavrentovich, Zh Eksp Teor Fiz **85**, 1997 (1983).
[53] P. Poulin and D. A. Weitz, Phys. Rev. E **57**, 626 (1998).
[54] J.-i. Fukuda, M. Yoneya, and H. Yokoyama, The European Physical Journal E **13**, 87 (2004), ISSN 1292-8941.
[55] M. Cavallaro, M. A. Gharbi, D. A. Beller, S. Čopar, Z. Shi, T. Baumgart, S. Yang, R. D. Kamien, and K. J. Stebe, PNAS **110**, 18804 (2013).
[56] M. A. Lohr, M. Cavallaro, D. A. Beller, K. J. Stebe, R. D. Kamien, P. J. Collings, and A. G. Yodh, Soft Matter **10**, 3477 (2014).
[57] D. Cheng, S. Sridharamurthy, J. Hunter, J.-S. Park, N. Abbott, and H. Jiang, Microelectromechanical Systems, Journal of **18**, 973 (2009).
[58] F. John, *Plane waves and spherical means applied to partial differential equations* (Dover Publications, 2004).